Structure- Activity Correlations for *Brønsted Acid*, *Lewis Acid* and *Photo- Catalysed Reactions* of Exfoliated Crystalline Niobium Oxides

Yusuke Koito,[‡] Gregory J. Rees,[†] John V. Hanna,[†] Molly M.J. Li,[‡] Yung-Kang Peng,[‡] Tim Puchtler,[§] Robert Taylor,[§] Tong Wang,[§] Hisayoshi Kobayashi,[‖] Ivo F. Teixeira,[‡] M. Abdullah Khan,[‡] Hannah T. Kreissl[‡] and S.C. Edman Tsang*[‡]

[‡]Inorganic Chemistry Laboratory, University of Oxford, South Parks Road, Oxford, Oxfordshire, OX1 3QR, UK

† Department of Physics, University of Warwick, Gibbet Hill Road, Coventry, CV4 7AL, UK

[§]Department of Physics, Clarendon Laboratory, University of Oxford, Oxford, OX1 3PU, UK

[‖] Department of Chemistry and Materials Technology, Kyoto Institute of Technology, Matsugasaki, Sakyo-ku, Kyoto, Japan

KEYWORDS Lewis and Brønsted acidity, Photo oxidation, Conduction band edge, Oxygen-Vacancy

ABSTRACT: Exfoliated crystalline niobium oxides containing exposed but interconnected NbO_6 octahedra with different degrees of structural distortions and defects have recently shown to catalyse Brønsted acid (BA), Lewis acid (LA) and Photo catalysed (PC) reactions efficiently but their structure-activity relationships are far from clear. Here, three exfoliated crystalline niobium oxides, namely $HSr_2Nb_3O_{10}$, $HCa_2Nb_3O_{10}$ and HNb_3O_8 are synthesised, extensively characterized and tested for selected BA, LA and PC reactions for the first time in a comparative manner. It is revealed that the three reactions show different structural origins: BA is found to associate mainly with acidic hydroxyl groups of edge shared NbO_6 octahedra as proton donors; LA to vacant band position of Nb^{5+} to receive electron pairs from substrate at excited state; PC to terminal Nb=O like of NbO_6 octahedra for photon capture and charge transfer to long-lived surface adsorbed substrate complex via associated oxygen-vacancy in close proximity. It is believed that such understanding of the structure-activity relationships could lead to tailored designs of NbOx catalysts for industrial important reactions.

Introduction

Niobium oxides possess many interesting physiochemical properties such as high water-tolerant Brønsted and Lewis acidities, semiconducting and photo and electrochromic properties which enable the materials for a wide variety of applications such as for gas sensing, catalysis, electronics, optical devices and displays.[1-4] The structures and morphologies of niobium oxides such as HNb_3O_8, $H_4Nb_6O_{17}$, $HSr_2Nb_3O_{10}$, $HCa_2Nb_3O_{10}$ and $HTiNbO_5$ can also be easily altered, which provide structural means to achieve tunable properties for these exciting applications.[5,6] Recently, it has been observed that exfoliated 2D niobium oxide structures with mostly exposed cation and anion sites exhibit more superior acid and photo catalytic performance than bulk materials. However, there is at present, a lack of understanding on their structure-activity relationships of the niobium oxides in correlating the above properties.

In general, solid acids are broadly classified into two types, Brønsted and Lewis acids. They exhibit different functions in acid catalytic reactions. The Brønsted acid is capable of transferring protons to substrate whereas Lewis acid facilitates the formation of a Lewis acid-substrate complex intermediate by the transfer of electron pairs in electrophile-nucleophile interaction, resulting in the polarization of the substrate. Consequently, Brønsted acidity can catalyse many hydrolysis and hydration reactions whilst Lewis acidity catalyses typical Meerwein-Ponndorf-Verley (MPV),[7] Baeyer-Villiger oxidation[8] and glucose isomerization[9] reactions. Niobium oxides possess both Brønsted and Lewis acid properties, which act as versatile catalysts to activate multistep reactions involving both acid functions. For instance, water-tolerant H_3PO_4-treated Nb_2O_5 can catalyse glucose transformation into 5-(hydroxylmethyl) furfural under mild reaction conditions.[10] But, there is still poor understanding on the chemical nature of Brønsted sites and the structural definition of Lewis acidity. Additionally, structural correlation with photocatalytic properties of niobium oxides is scarcely represented in the literature. It is generally thought to relate to electronic band structure, degree of oxygen-vacancy and efficiency of electron and hole-pairs generation under light irradiation, etc.[11] In some instances, these features and surface acidity of niobium oxide are somehow linked to achieve desirable redox reactions but no structural model is yet given. A substrate-Lewis acid sites surface complex structure has recently been proposed during the photo-oxidation reaction of benzylic alcohol on thin layer HNb_3O_8.[12] But no discussion is yet given how the photon is captured on a specific site of niobium oxide structure and how it subsequently leads to the formation of products.

In this paper, highly crystalline thin layers of related structures of exfoliated (ex) $HSr_2Nb_3O_{10}$, ex$HCa_2Nb_3O_{10}$ and exHNb_3O_8 were carefully synthesized through an exfoliation process (as shown in the Method section) from their respective bulk materials. These exfoliated sheets maintain the 2D crystal structures, forming precisely defined atomic structures. This can facilitate examination of the origins of solid Brønsted and Lewis acidity and more importantly photocatalysis in relation-

ships with these acidities based on an atomic scale and quantum chemical levels in comparative manner, which is not well understood for most solid acid materials. Thus, their structural integrities, degrees of distortion of octahedra and defects, acidities and band structures of these thin layered structures have been extensively characterized with XRD, multi-nuclear solid state NMR, EPR, XPS, CV, UV-vis, TRPL, etc. Model reactions including hydrolysis of ethyl acetate (Brønsted acid catalysed reaction); conversion of pyruvic aldehyde to lactic acid (Lewis acid catalysed reaction) and air oxidation of benzyl alcohol to benzylaldehyde and hydrogen production from water (photocatalysis) by niobium oxides have been examined, respectively. The structural aspects of the unique photocatalytic properties of these high surface 2-D layered niobium oxide structures are particularly discussed.

Experimental section

Materials and Synthesis

KNb_3O_8, $KSr_2Nb_3O_{10}$ and $KCa_2Nb_3O_{10}$ as chemical precursors were first synthesized by conventional solid state syntheses from their physical mixture using stoichiometric amounts of K_2CO_3, Nb_2O_5, Sr_2CO_3 and Ca_2CO_3.[13-15] The protonated forms were then produced by agitation of these obtained powders in excess 4M HCl solution repeatedly over 24 h. The preparation of exfoliated samples was conducted by using an intercalator reagent, the TBAOH (tetra butyl ammonium hydroxide) solution. The host crystals of HNb_3O_8, $HSr_2Nb_3O_{10}$ and $HCa_2Nb_3O_{10}$ possessing layer structures were held by acidic protons within their crystallographic planes. When they were soaked in aqueous TBAOH solution (pH > 11.0), the amine molecules were known to insert into each layers, resulting in layer segregation by weakening the interlayer stacking.[5,6] After centrifuging at 3,000 rpm for 5 min and the supernatant solution was mixed with 1M HNO_3, giving a white precipitate immediately. The obtained precipitate was then washed with distilled water until the pH of the filtrated solution became neutral and the sample was then dried at 80 °C.

As for the synthesis of the Pt nanoparticles, a mixture of hexachloroplatinic acid; $H_2PtCl_6{\bullet}6H_2O$ (62.1 mg), PVP (Mw=45000) (133 mg) and ethanol (180 ml) were refluxed for 3 h. The solvent was evaporated and the residue was dispersed into water/ethanol co-solvents ($V_{water}/V_{ethanol}$=1:1) (50 ml).[16] Pt loading on catalysts was prepared by sonicating the mixture of niobium oxides and Pt colloidal solution for 3 h. Following that this dispersed solution was centrifuged at 5000 rpm for 5 min and the obtained precipitate was washed by water and ethanol. Finally, the filtrated samples were naturally dried at ambient temperature for a few days. In order to remove the PVP residue the obtained samples were placed under UV irradiation, which led to photo-decomposition of the PVP layer that encapsulated the nanoparticles.[17]

Catalytic reactions

Hydrolysis of ethyl acetate into ethanol was carried out in a sealed Pyrex tube containing the mixture of ethyl acetate (1.9 mL), water (0.1 mL) and catalyst (0.12 mmol). After 20 h at 333 K, ethanol product was extracted into water layer by adding water (5 mL) into the product solution, followed by its analysis using high performance liquid chromatography (HPLC). Catalytic activities of exfoliated niobium oxides were examined for the conversion of pyruvic aldehyde to lactic acid in water. This reaction involved heating the mixture of catalyst (0.05 g) and 2.0 mL of aqueous pyruvic aldehyde (0.1 M) in a sealed Pyrex tube at 383 K for 2 h. The product solution was analyzed by HPLC. For photocatalytic oxidation of benzylic alcohol to benzylaldehyde reaction, a mixture of benzyl alcohol (0.0270 g), catalytst (20 mg) and benzotrifluoride (BTF) (7.5 mL) were stirred in a tight closed flask (25 mL) under UV irradiation for 20 h after the solution was pre-saturated with di-oxygen molecule. The resultant solution was then analyzed by ^{1}H NMR (Bruker Avance III HD nanobay 400MHz NMR).

For the hydrogen evolution experiments, the reaction was conducted by dispersed catalysts (20 mg) in a 100 mL co-solvent ((methanol (10 mL) and distilled water (90 mL)). Prior to that the solution was bubbled with 5% CH_4/Ar where CH_4 was used as an internal reference. This mixture was agitated under UV irradiation for 2 h and the obtained gas was analyzed by gas chromatography (Agilent 7890A) fitted with a Flame Ionisation Detector (FID).

NMR measurements

All solid state ^{93}Nb NMR spectra were recorded at 14.1 T (ν_0 = 146.71 MHz) and 19.9 T (ν_0 = 208.10 MHz) by Bruker Avance II+ and Avance III spectrometers, respectively. A Bruker static 5 mm broadband probe was used at each field. The spectra were referenced to the primary standard; saturated K[$NbCl_6$] in dry acetonitrile (δ_{iso} = 0 ppm).[18] A solid echo ($\pi/4 - \tau - \pi/4$) pulse sequence employing a 250 kHz non-selective pulse was utilised, with a relaxation time of 500 ms determined and a minimum of 4096 transients were collected for each experiment. The resonances with a width of over 250 kHz were collected via a variable offset cumulative frequency stepped (VOCS) method.[19,20] Spectral simulations were completed using the Topspin SOLA function. To fit the exfoliated samples, the isotropic shift (δ_{iso}) and broadening parameters where allowed to iterate whilst the CSA and quadrupolar determined interactions were fixed to the previously determined bulk crystal parameters (Table S2). If it was no longer viable to distinguish the resonance (due to the dramatic broadening caused by exfoliation), then that fit was removed from the deconvolution.

The ^{1}H MAS solid state NMR data was collected at 14.1 T (ν_0 = 599.44 MHz) by a Bruker Avance II+ spectrometer. A 30 kHz MAS frequency was facilitated by a Bruker 2.5 mm double air bearing HX probe. The spectra were referenced to the secondary standard alanine which gives three resonances at δ_{iso} = 1.1 (CH_3), 3.5 (CH) and 8.5 (COOH) ppm with respect to TMS (δ_{iso} = 0 ppm).

TRPL measurements

The sample was excited by a frequency-trippled Ti:Sapphire laser (266 nm) giving ~150 fs pulses with a repetition frequency of ~7.57 MHz. This beam was passed through a reflecting x36 objective lens (0.5 NA) onto the sample. The emitted signal was passed back through the same lens to an Andor Shamrock 303i spectrometer using an iDus 420 CCD. For time-resolved PL, the beam was directed to an output slit in the spectrometer (selecting a window of ~10 nm) and passed to a PMT detector (Becker and Hickl PMH-100, with an IRF ~ 200 ps) connected to a PicoQuant TimeHarp 260 TCSPC card (resolution 25 ps).

XPS measurements

XPS measurements were recorded on a Thermo Scientific K-Alfa XPS instrument equipped with micro-focused monochromated Al X-ray source. The source was operated at 12 keV and a 400 micron spot size was used. The analyzer operated at the analyzer energy (CAE) of 200 eV for survey scans and 50 eV for detailed scans. Charge neutralization was applied using a combined low energy/ ion flood source. The data acquisition and analysis were conducted with CasaXPS (Casa software Ltd.). The peak position was referenced to C1s peak of the carbon tape at 285.00 eV[21] and peak fitting was applied by using Lorentzian / Gaussian (L/G) 30 % curve.

UV-vis, XRD, BET surface area analyzer, Raman spectra, XPS, CV, EPR and TEM measurements

Crystalline phase of the samples were identified by powder XRD; X' pert Pro (PANalytical) operating in Bragg-Brentano focusing geometry and using Cuka radiation (λ= 1.5418 Å) from a generator operating at 40 kV and 40 mA. TEM images of the samples were recorded by JEOL 2010 electron microscope with a high resolution pole piece. The UV-vis adsorption spectra were recorded with UV-vis spectrometer (Lambda 750S, Perkin Elmer) with potassium bromide as the reference.

Specific surface area was derived from the corresponding adsorption isotherms with a conventional BET nitrogen adsorption apparatus (micromeritics 3flex). The samples were dried at 150 °C under vacuum for 24 h prior to the experiments.

Raman spectra were measured with via Raman Microscope (Renishaw) with a laser excitation wavelength of 532 nm. Exposure time of 10 sec and 8 number scans were adopted for each experiment. These samples were also dried at 150 °C before the measurements.

For CV measurements (Ivium, CompactStat), the scan was recorded by measuring the potential across the membrane hosting catalysts on the tip of electrode, which was prepared by drying the mixture of catalysts (10 mg), Nafion (Nafion D-521 dispersion, 5% w/w in water and 1-propanol, >0.92 meq/g exchange capacity) (10 µl) and milliQ water (1 ml) in order to stabilize the membrane. Electrolyte used was 0.1 M aqueous KCl solution. A sweeping voltage in the range of 0.3 V to -1.4 V at 50 mV s^{-1} was used.

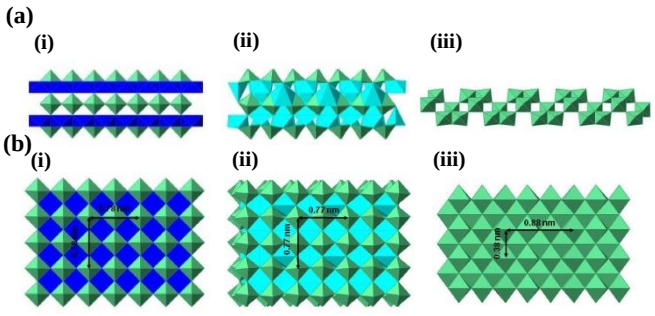

Figure 1. Two views (a, b) of crystal structures of niobium oxides of **(i)** $HSr_2Nb_3O_{10}$, **(ii)** $HCa_2Nb_3O_{10}$ and **(iii)** HNb_3O_8 according to ISCD database. GaussView5.0 was used to reproduce the structures. Atoms are colour labelled as follows: Nb (green), Sr (dark blue) and Ca (light blue).

Results and Discussion

Structural analysis of exfoliated niobium oxide layers

Fig. 1(a) shows the bulk Nb(IV) containing structures, $HSr_2Nb_3O_{10}$, $HCa_2Nb_3O_{10}$ and HNb_3O_8. The first two belong to the class of layered perovskite structures, $AB_2Nb_3O_{10}$ containing 12 ***corner shared NbO_6*** units with Sr^{2+} or Ca^{2+} at the B sites. These compounds consist of negatively charged perovskite sheets that stack to form a two-dimensional layered structure interleaved with H^+ in the A sites for compensation of the negative charge of sheets. It is noted from Figure 1(i) that Sr^{2+} ion (1.58 Å in 12 coordination) at the B site fits very well to the layered perovskite structure. However, the occupancy of smaller Ca^{2+} cations (ionic radius of 1.48 Å with higher charge density clearly reduce the dimensions of perovskite layer, decrease the symmetry (see Fig. 1(ii)) cause a substantial distortion to individual NbO_6 units with pronounced off-centre Nb^{5+} of a perfect octahedral geometry than that of larger Sr^{2+} ions.[22] On the other hand, apart from corner-sharing NbO_6 HNb_3O_8, the structure also contains ***edge-sharing NbO_6***[23] and the H^+ cations are emplaced between the 2D anion sheets. The XRD patterns of bulk and exfoliated $HSr_2Nb_3O_{10}$, $HCa_2Nb_3O_{10}$ and HNb_3O_8 samples were collected and are shown in Fig. 2(a). Notice that the intensities of (004) and (006) peaks due to layer stacking along z-axis for $exHSr_2Nb_3O_{10}$ and $exHCa_2Nb_3O_{10}$ significantly decrease after exfoliation although much broader and weaker (002) diffraction peaks are still observed even after the exfoliation process. This indicates that there was no long range layer stacking of the materials but thin exfoliated layers are produced. The TEM images of the exfoliated samples shown in Fig. 2(b) indeed depict the thin nanosheets morphology, where flake-like 2D nanosheets structure ranging from 1-8 layers is clearly evident for the samples.

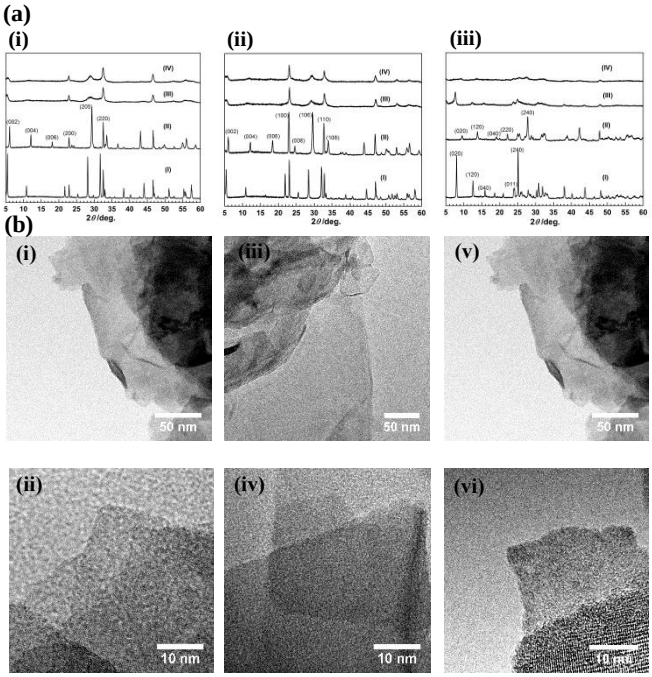

Figure 2. (a) XRD patterns of **(i)** $HSr_2Nb_3O_{10}$, **(ii)** $HCa_2Nb_3O_{10}$ and **(iii)** HNb_3O_8, :(I) hydrated crystal precursor, (II) formed from (I) by calcination at 150 °C for 3 h. (III) synthesized by exfoliation from (II) and (IV) formed from *(3)* by calcination at 150 °C for 3 h. **(b)** TEM and HRTEM images of $exHSr_2Nb_3O_{10}$ ((i) and (ii)), $exHCa_2Nb_3O_{10}$ ((iii) and (iv)) and $exHNb_3O_8$ ((v)

Proton sites on shared NbO_6 units and Brønsted acidity (BA)

The solid state ^{1}H MAS NMR (SSNMR) spectra shown in Fig. 3 (a), (c), (e) reflect the different chemical environment of protons in $HSr_2Nb_3O_{10}$, $HCa_2Nb_3O_{10}$ and HNb_3O_8, respectively, which are resident between the three bulk negatively charged crystalline niobium layer oxides of strongest BA in the range between 9.8 to 11.2 ppm. They have clearly shifted to lower frequencies along with weaker and broadened peak intensity, as observed in their exfoliated counterparts due to the collapse of the layer structures.[24,25] As a result, analysis of ^{1}H SSNMR spectroscopy can reflect the new chemical environment of surface attached protons on different degrees of connectivity of the NbO_6 octahedra over these different forms of exfoliated niobium oxides. For the surface exposed sheets, the ^{1}H chemical shift indicates acidity, and hydrogen species with a high downfield shift are expected to possess stronger Brønsted acidity. Clearly, the layered structure of $exHSr_2Nb_3O_{10}$ contains stacked NbO_6 octahedra in highest symmetry with primarily shared corners giving the lowest average proton chemical shift value (the distribution curve with the most probable peak at δ_{iso} = 4.6 ppm as shown in Fig. 3b) with the weakest BA (Fig. 3b). Comparatively, the structural distorted octahedra in the case $exHCa_2Nb_3O_{10}$ can give stronger BA sites (assigned peak at δ_{iso}= 6.3 ppm as shown in Fig. 3d). Conversely, the layered structure of HNb_3O_8 contains stacked NbO_6 octahedra with shared edges, giving a group of strongest BA amongst all the exofilated samples (assigned as δ_{iso}= 7.0 6.5 and 5.9 ppm in Fig. 3f). It is to note that the strongly acidic BA site on Group IV-VI oxides is associated with exposed bridging hydroxyl groups between octahedra with shared edges or faces while the weaker BA corresponds to a proton localized on a terminal oxygen.[24,25] According to the BET analysis (Fig. S1), $exHSr_2Nb_3O_{10}$, $exHCa_2Nb_3O_{10}$ and ex HNb_3O_8 give surface areas of 53, 56 and 112 m^2/g, respectively. Thus, the quantity and strength of Brønsted acidity follow $exHNb_3O_8$ > $exHCa_2Nb_3O_{10}$ > $exHSr_2Nb_3O_{10}$. It is noted that the activity for the BA catalyzed hydrolysis of ethyl acetate reaction[24] also gives the same order as above. The measured rates for ethanol production from ethyl acetate over $exHSr_2Nb_3O_{10}$, $exHCa_2Nb_3O_{10}$ and $exHNb_3O_8$ are 0.10, 0.12 and 0.20 μmol/min, respectively (Fig. 4).

Figure 3. The ^{1}H MAS (30 kHz) NMR at 14.1 T for **(a)** $HSr_2Nb_3O_{10}$, **(b)** $exHSr_2Nb_3O_{10}$ **(c)** $HCa_2Nb_3O_{10}$, **(d)** $exHCa_2Nb_3O_{10}$, (e) HNb_3O_8 and **(f)** $exHNb_3O_8$. The isotropic shift (δ_{iso}) are given above each resonances.

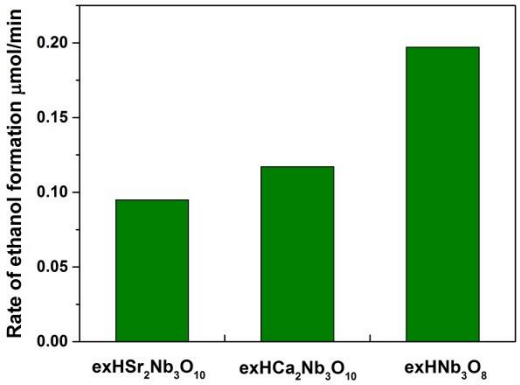

Figure 4. Catalytic performance of hydrolysis of ethyl acetate. A mixture of 1.9 mL ethyl acetate, 0.1 ml water and 50 mg catalyst was heated in a vacuum vial with fluoro-rubber cap at 333 K for 20 h.

Distorted NbO_6 units and Lewis acidity (LA)

In general, the position of LUMO of Lewis acid sites (cationic sites) are responsible for the formation of transient LA-nucleophilic reactant adduct that consequently, enhances LA catalytic reactions.[26] The LUMO energy can correspond to the conduction band edge in the solid catalyst, inferring that Lewis acids with lower energy of the conduction band edge are advantageous for activating Lewis acid catalyzed reaction.

Fig. 5 shows (a) UV-vis spectra for layered and exfoliated $HSr_2Nb_3O_{10}$, $HCa_2Nb_3O_{10}$ and HNb_3O_8 and (b) corresponding Kubelka-Munk plots against the energy of light. The estimated band gap energies of $exHSr_2Nb_3O_{10}$, $exHCa_2Nb_3O_{10}$ and $exHNb_3O_8$, are 3.30, 3.39, 3.29 eV, respectively.[27] Further, using the equation of $E_{CB} \approx 1.23-Eg/2$,[28] the lowest conduction band potential of each niobium oxides; $exHSr_2Nb_3O_{10}$, $exHCa_2Nb_3O_{10}$ and $exHNb_3O_8$ are estimated to −0.42, −0.47 and −0.42 eV. Interestingly, these results show that $exHCa_2Nb_3O_{10}$ has a more negative CB edge potential, presumably reflecting the degree of structural distortion of the NbO_6 units due to the polarization of the Ca^{2+} in B site. This observation matches with our EXAFS data (Table S1) which shows significant distortion of NbO_6 units to off-centre Nb^{5+} from perfect octahedral geometry, giving longer Nb-O bonds (2.51 Å) when facing the high charge density Ca^{2+} in B site in $exHCa_2Nb_3O_{10}$ (to maintain charge neutrality shorter Nb-O bonds of 1.66 Å are simultaneously created). The degrees of distortion for both $exHSr_2Nb_3O_{10}$ and $exHNb_3O_8$ are similar but marginal. Blasse *et al.* reported the relationship between crystal structures and energy delocalization of perovskite structures consisting of corner-sharing NbO_6 octahedral units.[29] According to their study, the relatively stronger interaction between NbO_6 octahedra with B cations results in localization of the excited state energy, because a bond angle of Nb–O–Nb is far from the ideal angle of 180°, i.e., the NbO_6 octahedral units are tilted. The localization of excited state energy clearly causes the position of absorption band edge to be shifted to shorter wavelength with weaker Lewis acidity.

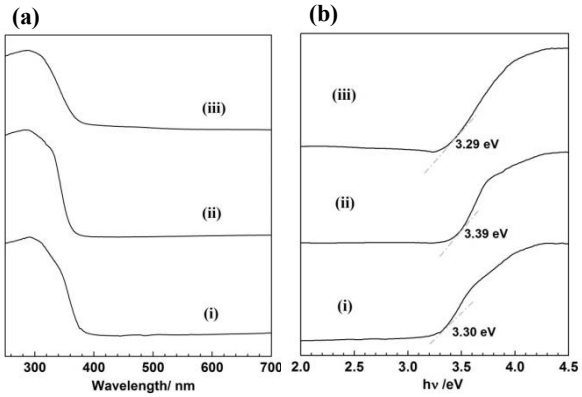

Figure 5. (a) UV-vis absorption spectra of **(i)** $exHSr_2Nb_3O_{10}$ **(ii)** $exHCa_2Nb_3O_{10}$ and **(iii)** $exHNb_3O_8$; **(b)** Transformed Kubelka-Muck plot versus energy of light of **(i)** $exHSr_2Nb_3O_{10}$ **(ii)** $exHCa_2Nb_3O_{10}$ and **(iii)** $exHNb_3O_8$

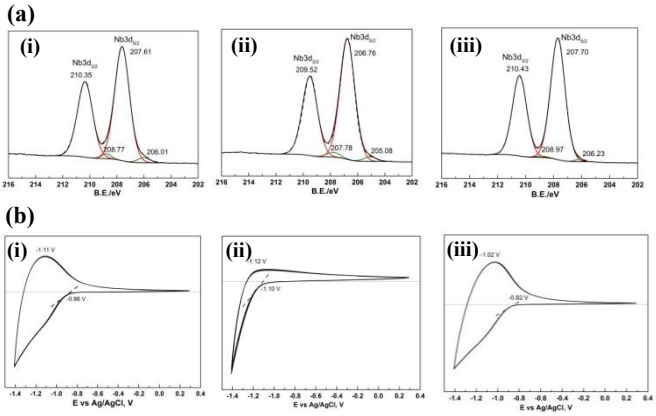

Figure 6. (a) XPS spectra of **(i)** $exHSr_2Nb_3O_{10}$, **(ii)** $exHCa_2Nb_3O_{10}$ and **(iii)** $exHNb_3O_8$. The spectra fitting was conducted by Casa XPS. **(b)** Cyclic voltammograms of $exHSr_2Nb_3O_8$, $exHCa_2Nb_3O_{10}$ and **(c)** $exHNb_3O_8$.

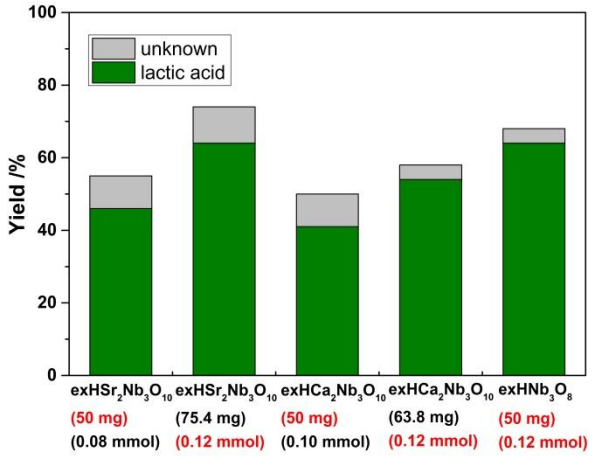

Figure 7. The catalytic yield of lactic acid from after 2h reaction over three exfoliated samples is shown. A mixture of catalyst (50 mg) and 2.0 mL aqueous pyruvic aldehyde solution (0.1 M) were heated in a vacuum vial with fluoro-rubber cap at 383 K. Comparison can be made with normalized quantity of catalysts (in mg or in mmol marked in red).

The chemical nature of niobium species has been further investigated by XPS as shown in Fig. 6(a). Note that the main signals of $Nb3d_{5/2}$ and $Nb3d_{3/2}$ of $exHSr_2Nb_3O_{10}$ and $exHNb_3O_8$ appear at slightly higher binding energy (BE) than that of $exHCa_2Nb_3O_{10}$. In case of $exHSr_2Nb_3O_{10}$ and $exHNb_3O_8$, BE of $Nb3d_{3/2}$ were seen at 210.35 eV and 210.43 eV, respectively and however, for $exHCa_2Nb_3O_{10}$, this peak was observed at 209.52 eV indicative of the more distorted and reduced nature of $exHCa_2Nb_3O_{10}$. Therefore, the conduction band level of Nb^{5+} in $exHCa_2Nb_3O_{10}$ is apparently higher compared to the other two exfoliated niobium oxide samples due to the polarization distortion of NbO_6 by the Ca^{2+}. Cyclic Voltammetry (CV) has also been used to probe the reduction potential of Nb^{5+} sites in $exHCa_2Nb_3O_{10}$. As shown in Fig. 6(b), the reduction potential of $exHNb_3O_8$ was −0.82 V (V vs V_{AgCl}), which is slightly higher than that of −0.86 V of $exHSr_2Nb_3O_{10}$. However, for the $exHCa_2Nb_3O_{10}$, it again shows that the significant lowest voltage of −1.10 V is required to reduce Nb^{5+} site in $exHCa_2Nb_3O_{10}$. As a result, from the correlation of conduction band energy level with Lewis acidity of the three exfoliated samples, the Lewis acidity order is expected to be $exHNb_3O_8 \geq exHSr_2Nb_3O_{10} >> exHCa_2Nb_3O_{10}$. This result is good agreement with the results of UV-vis, EXAFS and XPS, etc.

It is well-accepted that Lewis acids can promote the conversion of pyruvic aldehyde to lactic acid.[26] Their catalytic performance depends on the LUMO energy position in homogeneous Lewis acid site or the lowest conduction band position in solid Lewis acids.[26] Thus, this reaction can be used as a chemical probe to illustrate the effectiveness of the exfoliated niobium oxide samples. Fig. 7 shows the conversion of pyruvic aldehyde and yield of lactic acid over $exHSr_2Nb_3O_{10}$, $exHCa_2Nb_3O_{10}$ and $exHNb_3O_8$. Despite the small difference in catalytic activity of $exHSr_2Nb_3O_{10}$ and $exHNb_3O_8$, they consistently exhibit higher yield of lactic acid than $exHCa_2Nb_3O_{10}$ per gram or mole of sample per unit time. The apparent low catalytic performance of $exHCa_2Nb_3O_{10}$ can clearly be attributed to its higher conduction band energy due to structural distortion, which weakens the binding of pyruvic aldehyde to lead to lactic acid in the transition state. Thus, the polarization distortion of NbO_6 by B site cation appears to play an important role in determining the Lewis acidity of the layered Nb oxide structures.

Distorted NbO_6, Nb=O, lattice vacancies and photocatalysis

As stated, photocatalysis is a complex phenomenon and there is so far very little knowledge how the structures of exfoliated niobium oxides correlate to their photo-activity. However, it is believed that the samples must contain ‘chromophore’ groups that can capture appropriate photonic energy and transfer it to substrate-solid complex to catalyse chemical reactions at longer timescale. Thus, elucidations on the chemical nature of the ‘chromophore’ groups and the sites for substrate-solid complex are crucially important in understanding their structure-activity relationship in photocatalysis. It is also noted that this lifetime for this substrate-solid complex for energy transfer in redox manner in photocatalysis should be long enough to initiate typical chemical reactions (10^{-10} to 10^{-5} s).[30] Therefore, the formation of stable substrate-niobium oxide complexes via Lewis acid-base interaction would be considered to be preferable for an effective electron migration under UV irradiation. In addition, the contribution of oxygen-vacancy sites cannot be underestimated since trapping substrate onto oxygen-vacancy site favours binding stabilization.

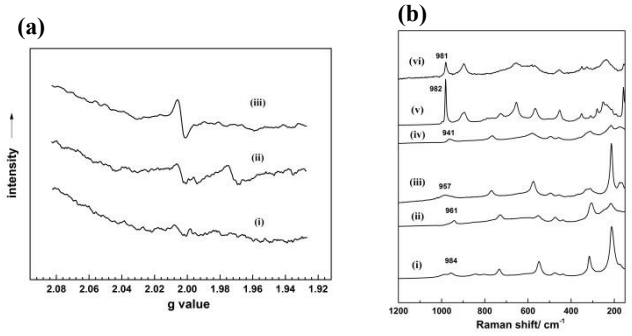

Figure 8. (a) ESR spectra of **(i)** $exHSr_2Nb_3O_{10}$, **(ii)** $exHCa_2Nb_3O_{10}$ and **(iii)** $exHNb_3O_8$ measured at ambient temperature. **(b)** Raman scattering spectra of **(i)** $HSr_2Nb_3O_{10}$ **(ii)** $exHSr_2Nb_3O_{10}$, **(iii)** $HCa_2Nb_3O_{10}$ **(iv)** $exHCa_2Nb_3O_{10}$, **(v)** HNb_3O_8, **(vi)** $exHNb_3O_8$.

First, ESR was used to demonstrate the formation of oxygen-vacancy sites in these exfoliated samples. As shown in Fig. 8(a), $exHNb_3O_8$ give a clear signal at g=2.01, which is assigned to free unpaired electron trapped in oxygen-vacancy site (O_v).[31] Only very weak or marginal signal is observed in $exHCa_2Nb_3O_{10}$ followed by $exHSr_2Nb_3O_{10}$. Therefore, oxygen-vacancy O_v sites were mainly produced in the $exHNb_3O_8$ structure with highest density of these three samples above. Interestingly, another small signal at g=1.98 is noted in $exHCa_2Nb_3O_{10}$, which could be assigned to the Nb^{4+}. The Nb^{4+} species generally give a very short spin relaxation time according to previous work.[32] This signal can only be confirmed at super-cold temperature (~4K).[33]

Fig. 8(b) shows the Raman spectra of bulk crystalline and exfoliated $HSr_2Nb_3O_{10}$, $HCa_2Nb_3O_{10}$ and HNb_3O_8. It is interesting to see the energetic lattice vibration of 950-990 cm^{-1}, which can be assigned to terminal Nb=O bond.[34] Thus, the signal of 961 cm^{-1} for $exHCa_2Nb_3O_{10}$ is apparently higher in wavenumber than that of $exHSr_2Nb_3O_{10}$ (941 cm^{-1}), presumably due to polarization distortion NbO_6 by the smaller size Ca^{2+} (B site) in the layer perovskite structure, as discussed. However, it is interesting to reveal that both bulk HNb_3O_8 and $exHNb_3O_8$ give the most intense and sharp signal at 981 cm^{-1} which clearly suggest the highest content of Nb=O. It is not yet known the reason why HNb_3O_8 structure can give rise to a higher degree of Nb=O (reflected by Raman) and O_v (reflected by ESR) defects presumably their formation may relate to the electronic and structural effects caused by the edge sharing octahedral (see SI). Such simultaneous formation of terminal Nb=O and O_v of NbO_6 in HNb_3O_8 structure could maintain the oxidation state of Nb (+5). Xiong *et al.* [35] have also recently reported the detection of Nb=O from Raman spectroscopy over their ultrathin Nb_3O_8 nanosheet. Based on the valence-shell electron-pair repulsion theory, they argued that the increasing Nb-O bond order will cause an enhanced repulsion effect on the Nb–O bond in the equatorial position of the octahedral NbO_6 structure. To release these repulsions, the charge centers of the Nb–O bond should be away from the central Nb atom, thus resulting in the stretching of the Nb–O bond, hence, facilitating the simultaneously generation of O_v defect from their nanosheet.

Static photo-luminescence (PL) and time resolved photo-luminescence (TRPL) analyses have therefore been conducted to reveal the fundamental photo-electron excitation and energy transfer processes in the time domain.

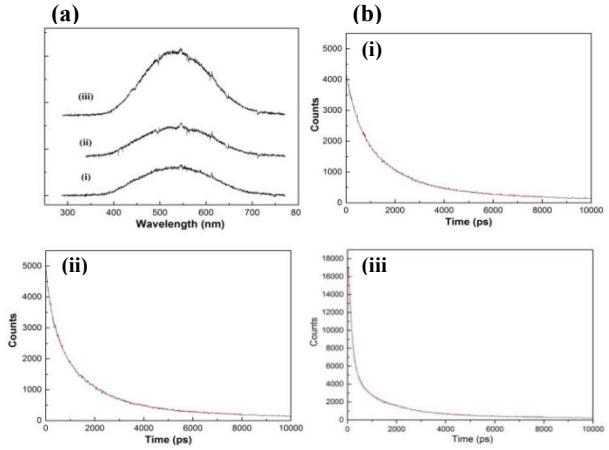

Figure 9. (a) PL spectra of **(i)** $exHSr_2Nb_3O_{10}$, **(ii)** $exHCa_2Nb_3O_{10}$ and **(iii)** $exHNb_3O_8$ and **(b)** TRPL spectra of **(i)** $exHSr_2Nb_3O_{10}$, **(ii)** $exHCa_2Nb_3O_{10}$ and **(iii)** $exHNb_3O_8$. The decay curve is fitted by a red line according to the following equation; $y=y_0+A_1\exp\left(\frac{-(x-x_0)}{t_1}\right)+A_2\exp\left(\frac{-(x-x_0)}{t_2}\right)$

Table 1. Experimental measured TRPL parameters of $exHNb_3O_8$, $exHSr_2Nb_3O_{10}$ and $exHCa_2Nb_3O_{10}$.

Catalyst	Fast Component		Slow Component	
	Decay Constant (ps)	Amplitude	Decay Constant (ps)	Amplitude
$exHSr_2Nb_3O_{10}$	552	1312	2033	1654
$exHCa_2Nb_3O_{10}$	343	1382	1796	2098
$exHNb_3O_8$	165	9861	1532	3408

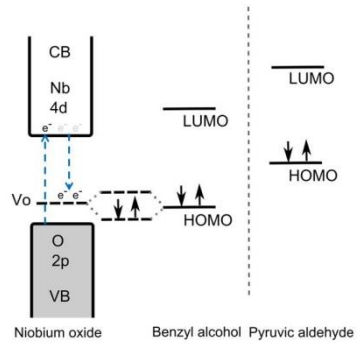

Scheme 1. Schematic of an energy diagram depicting CB edge (mainly contributed by vacant 4d band of Nb), VB edge (mainly contributed by filled O2p band) and oxygen-vacancies with electron transfer under UV irradiation and their relationship with HOMO levels of benzyl alcohol and pyruvic aldehyde.

Fig. 9(a) shows the PL spectra of $exHNb_3O_8$, $exHSr_2Nb_3O_{10}$ and $exHCa_2Nb_3O_{10}$. Clearly, $exHNb_3O_8$ with the highest content of Nb=O terminal bonds gives the highest PL signal 400-700 nm followed by $exHCa_2Nb_3O_{10}$ and then $exHSr_2Nb_3O_{10}$ upon 266 nm excitation. Thus, it is evident that Nb=O can act as a 'chromophore' to take up this photon energy which can then be transferred to radiative processes from 400- 700 nm through lattice relaxation. TRPL decay curves recorded during the UV irradiation are shown in Fig. 9(b). Table 1 summarizes the decay constants and amplitudes of each decay components. There is a fast decay component of the radiative recombination of the excited electrons and holes due to relaxation of the excited Nb=O structure. The relaxation times of excited Nb=O

bond in $exHNb_3O_8$, $exHCa_2Nb_3O_{10}$ and $exHSr_2Nb_3O_{10}$ are inversely related to their Raman vibration frequencies (Nb=O bond strength) as: (165 ps, 981 cm^{-1}), (343 ps, 961 cm^{-1}) and (552 ps, 941 cm^{-1}), respectively. On the other hand, there is also a slow decay observed, which is a component ascribed to the recombination of excited electrons and holes of Nb-O. The decay constant of the fast component is measured to be 165 ps of $exHNb_3O_8$, which is substantially faster than that of $exHSr_2Nb_3O_{10}$ (552 ps) and $exHCa_2Nb_3O_{10}$ (343 ps). In addition, its amplitude in the $exHNb_3O_8$ case is more than 7-fold higher than that of $exHSr_2Nb_3O_8$ and $exHCa_2Nb_3O_{10}$, again reflecting the Nb=O chromophore captures the photon energy and the larger amount gives a faster relaxation. In contrast, the slow components (τ~ 1.5- 2.0 ns) show no pronounced difference in terms of lifetime and amplitude for all the three exfoliated samples. It is thought that the co-existence of O_v in a close proximity in $exHNb_3O_8$ may offer a recombination centre or intermediate pathway for rapid relaxation of excited Nb=O after capturing photon energy, as shown in Scheme 1.

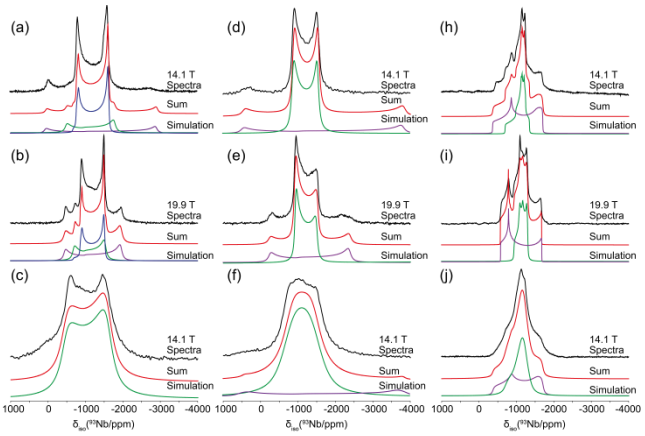

Interestingly, we note from Fig. 8(b) that there is no significant change of the Raman Nb=O peak of $exHNb_3O_8$ at 981 cm^{-1} in comparison to the bulk crystalline (982 cm^{-1}) although $exHSr_2Nb_3O_{10}$ and $exHCa_2Nb_3O_{10}$ show clear red shifts by 16 cm^{-1} and 23 cm^{-1}, respectively after exfoliation. The ^{93}Nb NMR spectra shown in Fig. 10 also provide similar structural information with that observed in Raman spectra. The exfoliation of the samples causes a decrease in the local symmetry; this gives a corresponding broadening in the ^{93}Nb spectra. The chemical shift of ^{93}Nb has been shown to depend on the oxygen coordination of the niobium site.[36] The large positive shift observed (~300 ppm) during exfoliation of the $HSr_2Nb_3O_{10}$ and $HCa_2Nb_3O_{10}$ complexes is attributed to the relaxation of NbO_6 units during the exfoliation process. In contrast, the $exHNb_3O_8$ spectra show no obvious shift. This result implies the formation of Nb=O terminal bonds stabilise the niobium site and prevent structural relaxation. It is noted from Table 2 that the broadening of the spectra after exfoliation for the $exHSr_2Nb_3O_{10}$ and $exHCa_2Nb_3O_{10}$ mean they can no longer be reliably deconvoluted to the substituted crystal sites. This is expected as the symmetry has been dramatically reduced due the distortion of the NbO_6 units. Conversely, despite the broadening of the $exHNb_3O_8$, the resonance can still be decovoluted into two niobium sites: this is expected as the formation of Nb=O terminal bonds would maintain some of the local symmetry. The ESR data (Fig 8(a)) shows an appreciable increase in oxygen vacancies for the $exHNb_3O_8$ sample, when compared to the lack of shift in the corresponding SSNMR and Raman data, it can be presumed that the oxygen vacancies also alleviate distortions of the NbO_6 units. As stated, many physiochemical properties of niobium oxides are derived from their structural distortion and presence of defect sites. The exposure of [NbO] sites by exfoliation is useful to enhance these properties provided that the structure is still maintained. Notably, the structure rigidity of HNb_3O_8 structure is clearly retained after the exfoliation process.

Table 2. Experimentally measured ^{93}Nb isotropic shift (δ_{iso}) data for the crystal and exfoliated samples. To determine the δ_{iso} the line broadening and shift parameters were allowed to iterate in the Topspin SOLA function, all other NMR interactions were kept constant. Where no δ_{iso} could be reasonably measured 'na' has been added to the table.

Niobate System	Site	δ_{iso}/ppm CRYSTAL	δ_{iso}/ppm EXFOLIATED
$HSr_2Nb_3O_{10}$	A	−981	Na
	B	−996	Na
	C	−1013	−794
$HCa_2Nb_3O_8$	A	−1053	Na
	B	−1055	−763
HNb_3O_8	A	−1072	−1063
	B	−1046	−1050

Fig. 11(a) shows the catalytic performance for the photo-oxidation of benzylalcohol to benzaldehyde[12] as a test reaction for the three exfoliated samples. The $exHNb_3O_8$ sample gives 41 % yield of aldehyde from the photo-oxidation of benzyl alcohol, which is significantly higher than that of $exHSr_2Nb_3O_{10}$ (18 %) and $exHCa_2Nb_3O_{10}$ (29 %) with the same amount of catalyst used (0.05 mmol). It is generally thought that substrate adsorption takes place mainly on a Lewis acid site in a photocatalyst.[12] However, Lewis acid catalysed reactions can be fundamentally different from photocatalysis. Particularly, the compatible timescale for photon energy transfer is crucially important in photocatalysis where stable complex between substrate-catalyst is required. In contrast, the Lewis acid site-substrate transition state at excited state does not need to couple with capture and transfer of photon energy. Interestingly, it is apparent that the order of Lewis acidity of the three exfoliated samples previously derived ($exHNb_3O_8 \geq exHSr_2Nb_3O_{10} >> exHCa_2Nb_3O_{10}$) is not consistent with the order of catalytic performance in this photo-oxidation reaction.

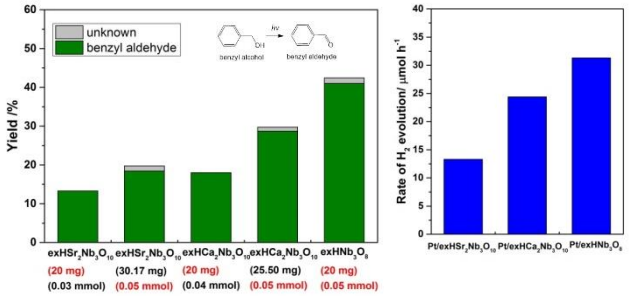

Similarly, photocatalytic hydrogen evolution over Pt loaded exfoliated samples has also been evaluated under UV excitation using sacrificial reagent (methanol).[35] No H_2 production was collected over the exfoliated samples without Pt. Fig. 11(b) clearly shows the results of hydrogen evolution rates in the presence of the three exfoliated samples upon irradiation. The catalytic rate order for the Pt loaded sample are $exHNb_3O_8$> $exHCa_2Nb_3O_{10}$> $exHSr_2Nb_3O_{10}$, which also corroborates well with that of photocatalytic oxidation of benzyl alcohol. We note that the photocatalysis of the two reactions clearly reflects the same order as their relative content of Nb=O and O_v. It is believed that the presence of Nb=O as 'chromophore' is responsible to capture the photon while the presence of O_v can offer trapping of oxygenated substrate.

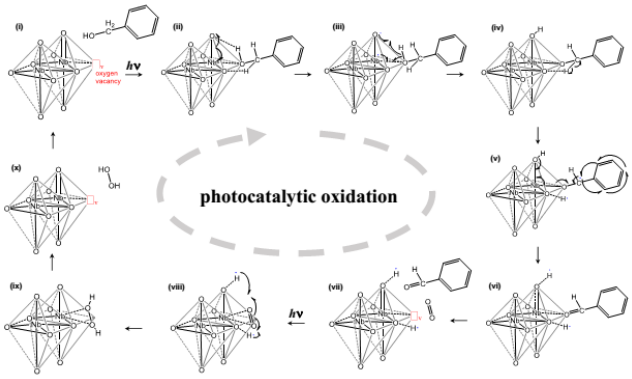

Scheme 2. Proposed reaction mechanism of benzyl alcohol oxidation over exfoliated niobium oxides under UV irradiation.

Considering the reaction scheme from energy perspective, it is argued that the introduction of O_v in $exHNb_3O_8$ can compete with the direct affinity for substrate of Lewis acidic Nb^{5+} to form a more stable substrate-catalyst complex. Particularly, conjugated carbonyl group from benzaldehyde is expected to give lower HOMO position than the reactive pyruvic aldehyde (Scheme 1). The high HOMO energy of pyruvic aldehyde is relatively favourable to interact with CB edge of Nb Lewis acid site directly but only at excited state whereas benzaldehyde is anticipated to interact relatively more easily with oxygen vacancy site at compatible energy level to effective binding of this substrate for sufficient time to induce photocatalysis.

As a result, Scheme 2 summarises a proposed mechanism of superior photocatalytic activity for benzyl alcohol oxidation over $exHNb_3O_8$ layers from this present study. First, the oxygen vacant site strongly binds the hydroxyl group in benzyl alcohol. This allows the 'chromophore' group (Nb=O) in close proximity to transfer its photon energy for chemical conversion. The UV photon energy captured by Nb=O produces excited electrons on Nb^{5+} Lewis acid site to interact with adsorbed benzyl alcohol specie via conjugated phenolic ring and prolongs charge separation in this stable LA-complex (photocatalytic reduction). Under this prolonged period of time, electron deficient terminal and bridging oxygens can abstract hydrogen atoms from the adsorbed benzyl alcohol as shown in the scheme. The activation of a di-oxygen molecule from the air by the regenerated oxygen vacant site after desorption of benzaldehyde can also take up the hydrogen atoms forming hydrogen peroxide as a side product (photocatalytic oxidation).[12] For the hydrogen evolution from water splitting, it is thought that for the capture of photons by Nb=O in $exHNb_3O_8$ allows the excited electrons to migrate to Pt surface (2 nm Pt particle, shown in Fig. S2) at the materials interface for catalytic reduction of H^+ in appropriate timescale[35] while the hole (positively charge terminal oxygen) will oxidise the adsorbed methanol at the prolonged relaxation time.

Conclusion

Exfoliated crystalline niobium oxides containing exposed but interconnected NbO_6 octahedra with different degrees of structural distortions and defects have been demonstrated to catalyse Brønsted acid (BA), Lewis acid (LA) and Photo catalysed (PC) reactions efficiently. It is shown that the catalytic performances of these reactions are highly dependent on the structural connectivity of the NbO_6 octahedra, their distortions and defects. Their structure-activity relationships are carefully studied in this comparative study. We believe that this work could lead to understanding and rational optimization of Nb oxides structures for more efficient catalysis in these reactions.

SUPPORTING INFORMATION

The Supporting Information regarding BET surface area analysis, TEM of Pt loaded samples, EXAFS results, ^{93}Nb NMR interaction parameters and theoretical calculation of binding energy, is available free of charge. (Fig. S1-S3 and Table S1-S3)

AUTHOR INFORMATION

Corresponding Author

* S.C. Edman Tsang (edman.tsang@chem.ox.ac.uk)

Present Addresses

†If an author's address is different than the one given in the affiliation line, this information may be included here.

ACKNOWLEDGMENT

We are grateful to the EPSRC for supporting the work at the University of Oxford. YK would like to acknowledge the postdoc-

toral funding from the Uehara Memorial Foundation Research Fellowship to enable him to work at Oxford. J.V.H. thanks the University of Warwick, EPSRC and the Birmingham Science City for access to the 14.1 T solid state MAS NMR instrumentation used in this research. The latter was funding obtained through the Birmingham Science City Advanced Materials Project 1: Creating and Characterising Next generation Advanced Materials project, with support from Advantage West Midlands (AWM) and the European Regional Development Fund (ERDF). In addition, J.V.H acknowledges the UK 850 MHz Solid State NMR National Facility also used in this research which was funded by EPSRC, BBSRC (contract reference PR140003) and the University of Warwick, which included partial funding through Birmingham Science City Advanced Materials Projects 1 and 2 supported by Advantage West Midlands (AWM) and the European Regional Development Fund (ERDF). Collaborative assistance from the UK 850 MHz Facility Manager (Dinu Iuga, University of Warwick) is also acknowledged.

Notes

The authors declare no competing financial interest.

REFERENCES

(1) (a) Zhao, Y.; Eley, C.; Hu, J.; Foord, J. S.; Ye, L.; He, H.; Tsang, S. C. *Angew. Chem.* **2012**, *51*, 3846. (b) Zhao, Y.; Zhou, X.; Ye, L.; Tsang, S. C. E. *Nano Rev*., **2012**, *3*, 17631. (c) Nakagawa, K.; Jia, T.; Zheng, W.; Fairclough, S. M.; Katoh, M.; Sugiyama, S.; Tsang, S. C. E. *Chem. Commun*., **2014**, *50*, 13702. (d) Kreissl, H. T.; Nakagawa, K.; Peng, Y-K; Koito, Y.; Zheng, J.; Tsang, S. C. E. *J. Catal.* **2016**, *338*, 329.

(2) Varghese, B.; Haur, S. C.; Lim, C. T. *J. Phys. Chem. C* **2008**, *112*, 10008.

(3) Yao, D. D.; Rani, R. A.; O'Mullane, A. P.; Kalantar-zadeh, K.; Ou, J. Z. *J. Phys. Chem. C* **2014**, *118*, 476.

(4) Rani, R. A.; Zoolfakar, A. S.; Ou, J. Z.; Field, M. R.; Austin, M.; Kalantar-zadeh, K. *Sens. Actuators B Chem.* **2013**, *176*, 149.

(5) Dias, A.; Lima, S.; Carriazo, D.; Rives, V.; Pillinger, M.; Valente, A. *J. Catal.* **2006**, *244*, 230.

(6) Tagusagawa, C.; Takagaki, A.; Hayashi, S.; Domen, K. *J. Phys. Chem. C* **2009**, *113*, 7831.

(7) Corma, A.; Domine, M. E.; Valencia, S. *J. Catal.* **2003**, *215*, 294.

(8) Renz, M.; Blasco, T.; Corma, A.; Fornés, V.; Jensen, R.; Nemeth, L. *Chem. Eur. J.* **2002**, *8*, 4708.

(9) Román-Leshkov, Y.; Moliner, M.; Labinger, J. A.; Davis, M. E. *Angew. Chem.* **2010**, *49*, 8954.

(10) Nakajima, K.; Baba, Y.; Noma, R.; Kitano, M.; Kondo, J. N.; Hayashi, S.; Hara, M. *J. Am. Chem. Soc.* **2011**, *133*, 4224.

(11) Niu, G.; Guo, X.; Wang, L. *J. Mater. Chem. A* **2015**, *3*, 8970.

(12) Liang, S.; Wen, L.; Lin, S.; Bi, J.; Feng, P.; Fu, X.; Wu, L. *Angew. Chem.* **2014**, *53*, 2951.

(13) Ban, T.; Yoshikawa, S.; Ohya, Y. *J. Colloid Interf. Sci.* **2011**, *364*, 85.

(14) Han, Y.-S.; Park, I.; Choy, J.-H. *J. Mater. Chem.* **2001**, *11*, 1277.

(15) Saruwatari, K.; Sato, H.; Idei, T.; Kameda, J.; Yamagushi, A.; Takagaki, A.; Domen, K. *J. Phys. Chem. B* **2005**, *109*, 12410.

(16) Rioux, R. M.; Song, H.; Hoefelmeyer, J. D.; Yang, P.; Somorjai, G. A. *J Phys. Chem. B* **2005**, *109*, 2192.

(17) Baker, L. R.; Kennedy, G.; Van Spronsen, M.; Hervier, A.; Cai, X.; Chen, S.; Wang, L. W.; Somorjai, G. A. *J. Am. Chem. Soc.* **2012**, *134*, 14208.

(18) Harris, R. K.; Becker, E. D.; Cabral de Menezes, S. M.; Goodfellow, R.; Granger, P. *Magn. Reson. Chem.* **2002**, *40*, 489.

(19) Akatsuka, K.; Takanashi, G.; Ebina, Y.; Haga, M.; Sasaki, T. *J. Phys. Chem. C* **2012**, *116*, 12426.

(20) Rees, G. J.; Orr, S. T.; Barrett, L. O.; Fisher, J. M.; Houghton, J.; Spikes, G. H.; Theobald, B. R.; Thompsett, D.; Smith, M. E.; Hanna, J. V. *Phys. Chem. Chem. Phys.* **2013**, *15*, 17195.

(21) Descostes, M.; Mercier, F.; Thromat, N.; Beaucaire, C.; Gautier-Soyer, M. *Appl. Surf. Sci.* **2000**, *165*, 288.

(22) Maeda, K.; Mallouk, T. E. *J. Mater. Chem.* **2009**, *19*, 4813.

(23) Akatsuka, K.; Takanashi, G.; Ebina, Y.; Sakai, N.; Haga, M.; Sasaki, T. *J. Phys. Chem. Solids* **2008**, *69*, 1288.

(24) Takagaki, A.; Sugisawa, M.; Lu, D.; Kondo, N. J.; Hara, M.; Domen, K.; Hayashi, S. *J. Am. Chem. Soc.* **2003**, *125*, 5479.

(25) Takagaki, A.; Lu, D.; Kondo, N. J.; Hara, M.; Hayashi, S.; Domen, K. *Chem. Mater.* **2005**, *17*, 2487.

(26) Koito, Y.; Nakajima, K.; Kobayashi, H.; Hasegawa, R.; Kitano, M.; Hara, M. *Chem. Eur. J.* **2014**, *20*, 8068.

(27) López, R.; Gómez, R. *J. Sol. Gel. Sci. Tech.* **2012**, *61*, 1.

(28) Matsumoto, Y. *J. Solid State Chem.* **1996**, *126*, 227.

(29) (a) Wiegel, M.; Emond, M. H. J.; Stobbe, E. R.; Blasse, G. *J. Phys. Chem. Solids* **1994**, *55*, 773. (b) Blasse, G.; de Haart, L. G. J.; *Mater. Chem. Phys*. **1986**, *14*, 481.

(30) Linsebigler, A. L.; Lu, G.; Yates Jr, J. T. *Chem Rev* **1995**, *95*, 735.

(31) Liao, F.; Huang, Y.; Ge, J.; Zheng, W.; Tedsree, K.; Collier, P.; Hong, X.; Tsang, S. C. *Angew. Chem.* **2011**, *50*, 2162.

(32) Folli, A.; Bloh, J. Z.; Lecaplain, A.; Walker, R.; Macphee, D. E. *Phys. Chem. Chem. Phys.* **2015**, *17*, 4849.

(33) Kiwi, J.; Suss, J. T.; Szapiro, S. *Chem. Phys. Lett.* **1984**, *106*, 135.

(34) Burcham, L. J.; Datka, J.; Wachs, I. E. *J. Phys. Chem. B* **1999**, *103*, 6015.

(35) Xiong, J.; Wen, L.; Jiang, F.; Liu, Y.; Liang, S.; Wu, L. J. Mater. Chem. A 2015, 3, 20627.

(36) Hanna, J. V.; Pike, K. J.; Charpentier, T.; Kemp, T. F.; Smith, M. E.; Lucier, B. E.; Schurko, R. W.; Cahill, L. S. Chem. Eur. J. 2010, 16, 3222.

Authors are required to submit a graphic entry for the Table of Contents (TOC) that, in conjunction with the manuscript title, should give the reader a representative idea of one of the following: A key structure, reaction, equation, concept, or theorem, etc., that is discussed in the manuscript. Consult the journal's Instructions for Authors for TOC graphic specifications.

Insert Table of Contents artwork here